WILEY VCH

Constructing Water-Stable Porous Organic Salts via Suppressed Proton Integration Using Fluorinated Tetrazole Tectons

Errui Li,[a,b] Xian Suo,[c] Yujing Tong,[d] Phattananawee Nalaoh,[a] David M. Jenkins,[a] Carlos Alberto Steren,[a] Lilin He,[e] Alexander S. Ivanov,[b] Leighanne C. Gallington,[f] Victoria Cooley,[f] Bo Li,[d] Xin Wang,[b] Kai Li,[g] Juntian Fan,[b] Liqi Qiu,[a] De-en Jiang,[d] Katie Johnson,[h] Shannon M. Mahurin,[b] Zhenzhen Yang,*[b] and Sheng Dai*[a,b]

[a] Dr. E. Li, Dr. P. Nalaoh, Dr. D. M. Jenkins, Dr. C. A. Steren, Dr. L. Qiu, Dr. S. Dai
Department of Chemistry, University of Tennessee Knoxville, Knoxville, TN 37996, USA

[b] Dr. E. Li, Dr. X. Wang, Dr. J. Fan, Dr. S. Mahurin, Dr. Z. Yang, Dr. S. Dai
Chemical Sciences Division, Oak Ridge National Laboratory, Oak Ridge, TN 37831, USA
E-mail: dais@ornl.gov; yangz3@ornl.gov

[c] Dr. X. Suo
ZJU-Hangzhou Global Scientific and Technological Innovation Center, Hangzhou, Zhejiang, China

[d] Y. Tong, Dr. B. Li, Dr. D. Jiang
Department of Chemical and Biomolecular Engineering, Vanderbilt University, Nashville, TN 37235, USA

[e] Dr. L. He
Neutron Scattering Division, Oak Ridge National Laboratory, Oak Ridge, TN 37831, USA

[f] Dr. L. C. Gallington, Dr. V. Cooley
X-Ray Science Division, Advanced Photon Source, Argonne National Laboratory, Lemont, IL 60439, USA

[g] Dr. K. Li
Buildings and Transportation Science Division, Oak Ridge National Laboratory, Oak Ridge, TN 37831, USA

[h] Dr. K. Johnson
Nuclear Energy and Fuel Cycle Division, Oak Ridge National Laboratory, Oak Ridge, TN 37831, USA

Supporting information for this article is given via a link at the end of the document.

Abstract: Porous organic salts (POSs) are an emerging class of materials with ordered ionic architectures, offering excellent proton transfer and water uptake properties. However, conventional POS synthesis via strong acid-base neutralization (e.g., -SO_3H and -NH_2) leads to extensive hydrogen bonding with water, compromising stability in aqueous and water-lean environments. Here, we address this challenge by designing POSs with hydrophobic porous channels and minimal hydrogen bonding formation. Our key innovation is the use of fluorinated tetrazole as a weak acid tecton and a tetra-substituted imidazole precursor devoid of active protons as the base. Single-crystal analysis and computational modeling reveal that the structural integrity of the synthesized POSs arises primarily from cation-anion interactions, with water confined as clusters in the pores, independent of hydrogen bonding with the scaffold. Robustness of the POS structure under aqueous and water-lean conditions is confirmed by X-ray and neutron scattering, as well as computational modeling, confirming preserved packing and crystal structures. The stability of POS is further demonstrated in aqueous iodine capture, with imidazolium cations and C–F functionalizations serving as strong adsorption sites. The approach developed herein further pushes the boundary of POS materials to withstand both aqueous and water-lean conditions.

Introduction

Porous crystalline materials featuring ordered architectures, diverse structures, and tunable properties have demonstrated attractive applications in separation, catalysis, energy storage, and beyond.[1-5] They can be classified as metal-organic frameworks (MOFs),[6-8] coordination cages,[9-10] covalent organic frameworks (COFs);[11-14] hydrogen-bonded frameworks (HOFs),[15-17] porous organic cages (POCs),[18-21] and porous organic salts (POSs),[19, 22] through the coordination-, covalent-, hydrogen-, and ionic-bond formation respectively. Particularly, the discovery of POSs has opened a new platform to construct porous crystalline scaffolds possessing abundant ionic sites.[23-24] POSs are generally synthesized via facile and catalyst-free neutralization approach and connected by strong ionic bond interaction using rigid and multiple substituted organic acid and base as precursors.[25] The highly polarized and ionic nature of POSs leads to attractive performance in proton transfer, water uptake, and diverse separation procedures.

The ordered and porous scaffolds of POSs were ensured by synergistic effect from cation-anion bridge and charge-enhanced hydrogen bonding formation. To allow strong ionic bond formation, synthons for POSs construction are generally selected from tectons with strong acidity and basicity.[26-28] For instance, acid tectons with sulfonic acid groups (-SO_3H) and low pKa values (-1.45) were widely adopted to drive the neutralization process.[29] Correspondingly, both aromatic and aliphatic amines (pKa value of 6.08 and 10.78 respectively) were used as the base counterparts. The neutralization reaction of -SO_3H and -NH_2 led to the formation of abundant ammonium cations paired with

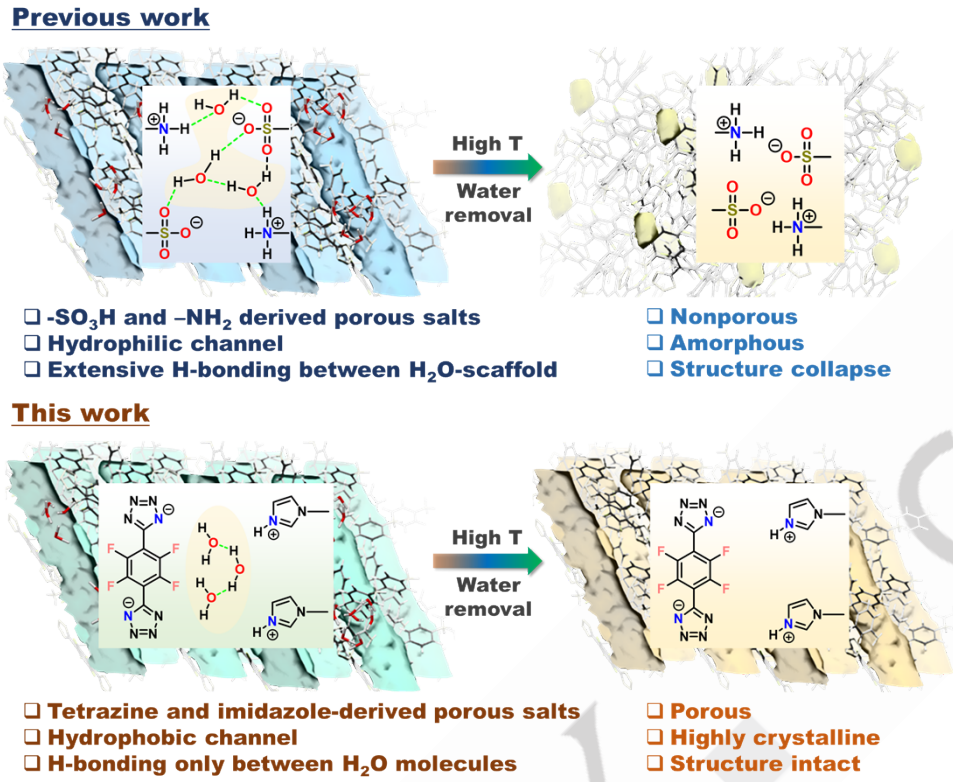

Figure 1 Comparison of water molecule integration and existing form in previously developed POSs versus those synthesized in this work, highlighting the exclusive internal hydrogen bonding between water molecules and the enhanced robustness of fluorinated tetrazine-derived POSs upon water removal.

sulfonate anions within the POS scaffolds. Additionally, the ordered architecture of POSs was maintained by the extensive hydrogen bonding network formed between the trapped H_2O molecules and scaffolds, as the ammonium cations and sulfonate anions are strong hydrogen-bonding donors and acceptors respectively. The critical role of integrated water molecules and extensive hydrogen bonding connections was further elucidated in POSs involving ammonium halide couples using organic cage tetons.[30-33]

Although current approaches utilizing strong acid-base neutralization and extensive hydrogen bonding network formation with H_2O have enabled the construction of POSs with crystalline architectures, their strong dependence on H_2O compromises stability at elevated temperatures and H_2O-involved environments (humid and aqueous).[34] Upon water removal at elevated temperatures, structural collapse of POSs occurs, resulting in amorphous and nonporous scaffolds (Figure 1). On the other hand, the highly hydrophilic nature of POSs limited their applications in humidity- or aqueous phase-involved separation procedures, as water molecules can easily penetrate into the porous channels, disturb the hydrogen bonding networks, and weaken the ionic interaction, leading to collapse of the scaffolds and performance decay.[35] Moreover, the highly polar nature of strong organic acid and base monomers necessitates H_2O addition for solubilization during crystallization. This presents a dilemma, while H_2O is essential for synthesis, it becomes an integral part of the POSs scaffold and cannot be removed without compromising structural integrity. Introducing multiple fluorine atoms into the skeleton of POSs could improve their water resistance,[36] as the hydrophobicity of fluorine moieties can help create a hydrophobic local environment around the hydrogen bonding sites. Still, the inherent stability highly relied on H_2O-involved hydrogen bonding network formation. Although the unique features of POSs make them promising for separation and energy storage applications,[27, 29, 37-38] there remains a lack of facile approaches to synthesize POSs with sufficient robustness to withstand both water-lean and aqueous conditions. A key challenge lies in designing tectons with weak hydrogen-bonding formation capabilities and hydrophobic properties to enhance structural stability.

Herein, we address the inherent instability of POS materials by designing ionic scaffolds with hydrophobic porous channels and minimal hydrogen bonding formation (Figure 1). The robust POS framework was constructed using fluorinated tetrazole (H_2FBTB) as a weak acid tecton and tetrakis(1-imidazolyl)borate (TIBS), a base devoid of active protons (Figure 2). The structural integrity of the synthesized TPOS-1 is primarily governed by statistical cation-anion interactions, with water molecules confined as clusters in channels without hydrogen bonding formation with the scaffold. Its stability under both aqueous and water-lean (high-temperature) conditions was confirmed by X-ray and neutron scattering techniques, revealing well-preserved packing mode and bonding structures independent of water molecules. In contrast, the control material, TPOS-2, synthesized via neutralization of H_2FBTB with tetrakis-(4-aminophenyl)methane (TAPM), exhibited extensive hydrogen bonding network between water molecules and the scaffold. This led to severe structural distortion upon exposure to humidity or removal of water. The enhanced stability of TPOS-1 enables its application in aqueous phase iodine capture, demonstrating high

uptake capacity and good recyclability, with imidazolium cations and benzene rings serving as key binding sites. This approach broadens the scope of POS materials to function effectively under both aqueous and dry conditions.

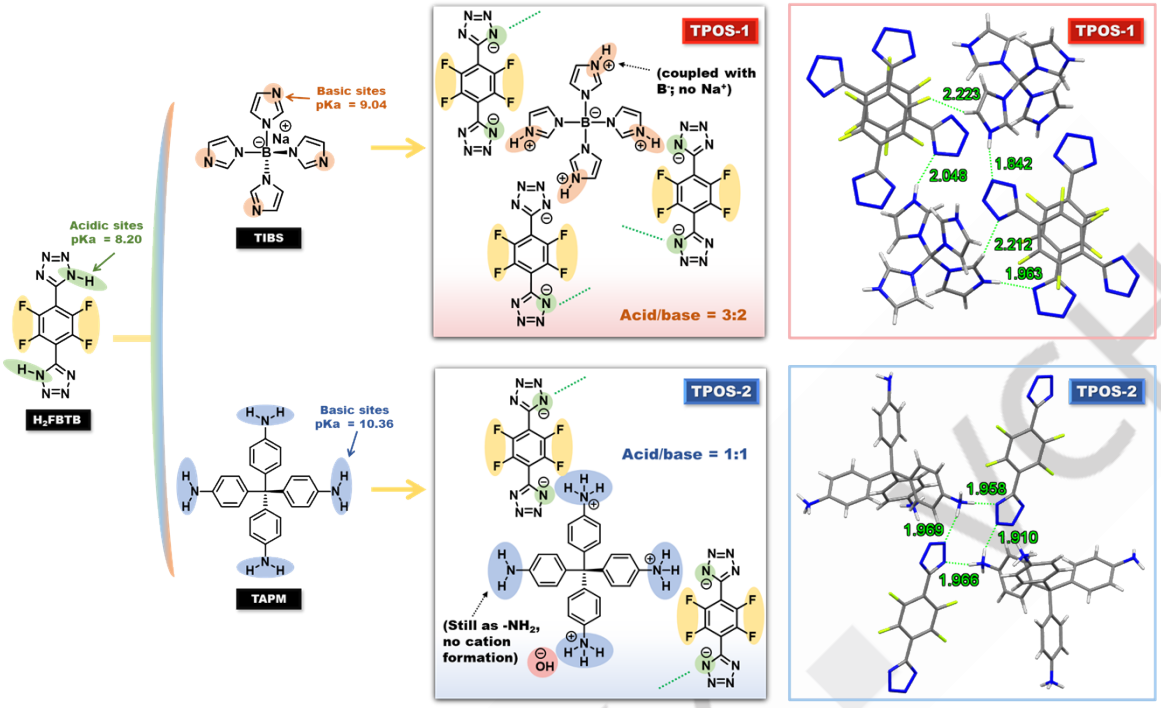

Figure 2. Structures of the organic acid (H_2FBTB) and base (TIBS and TAPM) tectons in TPOS-1 and TPOS-2 construction based on new types of salt bridge connection via neutralization reaction. Structures of TPOS-1 and TPOS-2 herein were determined by single crystal characterization.[54]

Results and Discussion

To construct POSs with enhanced temperature and water resistance, acid and base tectons with hydrophobic moieties and weak proton-donating and -accepting abilities are promising candidates. Herein, 1,4-bis(1H-tetrazol-5-yl)tetrafluorobenzene (H_2FBTB) was selected as the C_2 tecton (Figure 2), in which the proton in the tetrazole unit (only one per unit) serves as an acid site, with a pKa of 8.20 in water (measured by titration; see SI for details). Since the pKa is below 10, these protons contribute to the compound's acidity.[39-40] Additionally, the fluorinated benzene ring provides a potential hydrophobic local environment. Notably, acidity of the proton in H_2FBTB was much weaker than that in sulfonic acid moieties (pKa = -1.45).[29] Correspondingly, sodium tetrakis(1-imidazolyl)borate (TIBS) was utilized as the tetrahedral (T_d) tecton to provide the base sites, of which the pKa value in water reaches 9.04 and the basicity was enough to drive the deprotonation of H_2FBTB (acid tecton). Particularly, no active protons were involved in the structure of TIBS, which can limit the hydrogen bonding formation sites in the as-afforded POS. For comparison and to elucidate the effect of hydrogen bonding formation on the stability of POSs with structure similarity, the other organic base tetrakis-(4-aminophenyl)methane (TAPM) (pKa = 10.36 in water), with extra active protons were also deployed for POS construction by reacting with H_2FBTB.

POSs were prepared by dissolving the organic acid and base tecton couples in mixed solvents, followed by crystallization (see details in SI). The deprotonation of H_2FBTB by TIBS and TAPM afforded TPOS-1 and TPOS-2, respectively. The structural information was obtained by single crystal X-ray diffraction (SC-XRD) analysis (Figure 2). Crystal structure analysis demonstrated that TPOS-1 is composed of H_2FBTB and TIBS units in a molar ratio of 3:2. The scaffold was connected via the tetrazolate-imidazolium ionic pairs and π-π stacking interaction. Charge-enhanced intermolecular hydrogen bonding was only observed around the protons on the imidazolium cations, which were created via proton transfer from the tetrazole of H_2FBTB to imidazole of TIBS. While the original sodium ions in TIBS was not observed in the TPOS-1 framework, indicating that the sodium ions exchanged protons with the water solvent (Table S1). Similarly, the TPOS-2 was fabricated from the mixture of H_2FBTB and TAPM. Its crystal structure showed that the molar ratio of H_2FBTB and TAPM is 1:1 (Figure 2). Besides, the proton on the tetrazole of H_2FBTB transferred to the amine group of TAPM, forming charge-enhanced intermolecular hydrogen bonding. Meanwhile, proton transfer from water molecules to the amine groups was also observed, forming ammonium cation paired with hydroxide anion.

The powder X-ray diffraction (PXRD) pattern of the as-synthesized TPOS-1 was in good agreement with that simulated from the single crystal structure (Figure 3a). Views along the *b* and *c* axes reveal that the channel edges are primarily populated

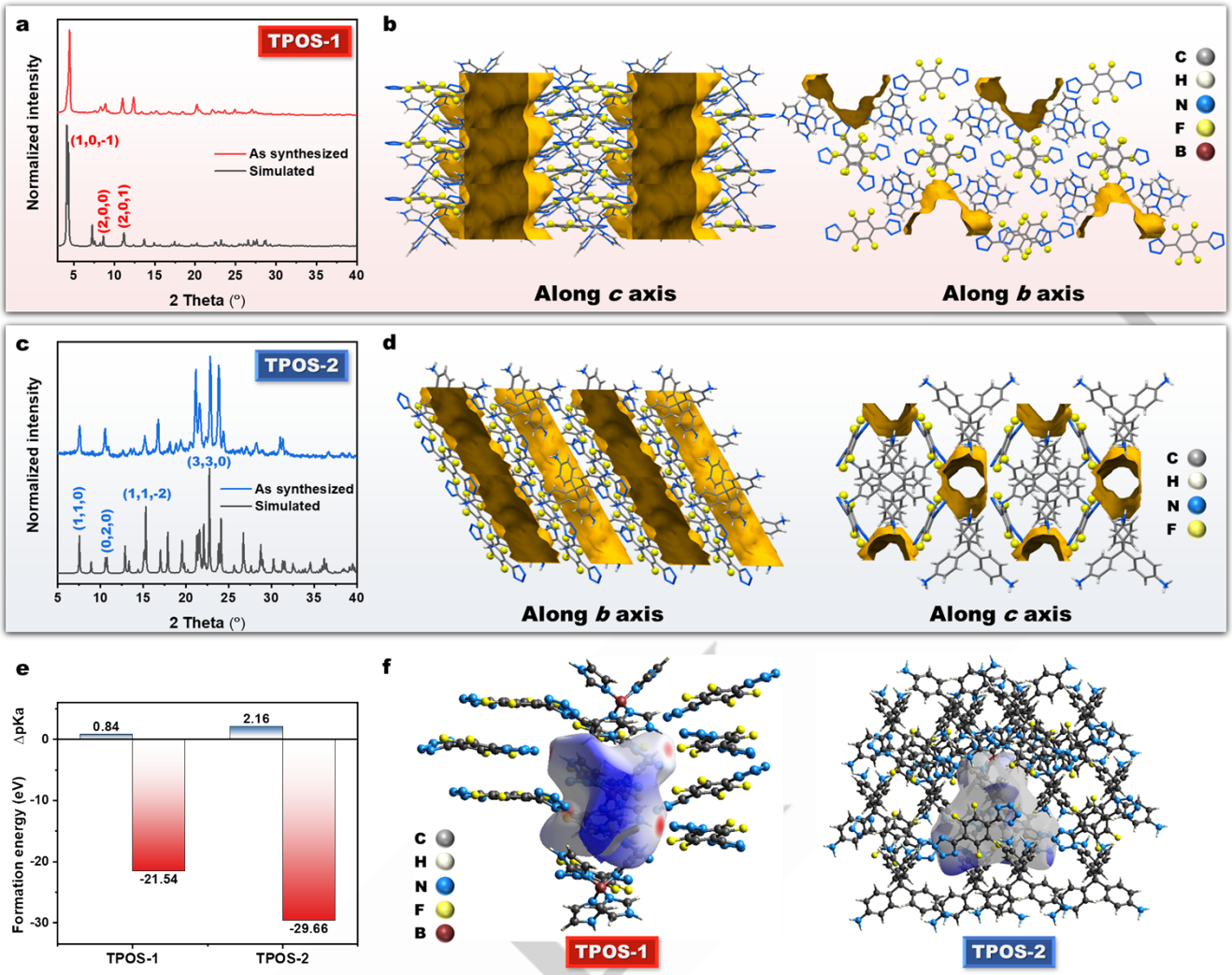

Figure 3. (a) PXRD patterns of TPOS-1 powder and that simulated from the single crystal structure. (b) Crystal structures of TPOS-1 along b and c axis highlighting scaffold structures around porous channels (Solvent molecules are omitted for clarity). (c) PXRD patterns of TPOS-1 powder and that simulated from the single crystal structure. (d) Crystal structures of TPOS-2 along b and c axis highlighting peripheral structures of porous channels (Solvent molecules are omitted for clarity). (e) Comparison of ΔpKa (blue) and formation energy (red) for TPOS-1 and TPOS-2. (f) Hirshfeld surfaces of TPOS-1 and TPOS-2 indicating the interaction strength between TIBS anion and adjacent cations.

by polar tetrazole and imidazole groups, while the C-F moieties are positioned at a greater distance from the channel (Figure 3b). The PXRD pattern of the as-synthesized TPOS-2 also matched well with that simulated from the corresponding single crystal structure (Figure 3c), indicating its good crystallinity and phase purity. Notably, fluorine atoms and tetrazole groups are positioned at the edges of the cavity channels, while extensive hydrogen bonding is present in the dense scaffold region (Figure 3d). The atomic-scale structure of the material in real space was further explored using the pair distribution function (PDF) technique, based on synchrotron X-ray scattering measurements.[41-43] The experimentally obtained PDF, denoted as G(r), for both TPOS closely matched the simulated G(r) derived from its single crystal structure (Figures S1–S4). In TPOS-1, the first prominent peak at 1.39 Å was primarily attributed to nearest-neighbor F–C, N–C, N–N, and C–C atomic pairs, as supported by the radial distribution functions (Figure S5). For TPOS-2, the first peak appeared at 1.37 Å and was similarly assigned to N–N, C–C, N–C, and F–C correlations (Figure S6). Additional intense peaks at longer distances (2.43 Å and 2.85 Å in TPOS-1, and 2.24 Å and 3.64 Å in TPOS-2) were indicative of extended atomic correlations beyond the nearest neighbors.

The formation energies of TPOS-1 and TPOS-2 were calculated starting from different tecton pairs via the density functional theory (DFT). Despite the ΔpKa between TIBS and H_2FBTB being only 0.84, a formation energy of -21.54 eV for TPOS-1 is obtained (Figure 3e). For TPOS-2, a more negative formation energy of -29.66 eV is obtained, which is attributed to the relatively large ΔpKa of 2.16 between TAPM and H_2FBTB. Further analysis revealed that the dominating bonding

interactions in TPOS-1 and TPOS-2 have significant differences. Hirshfeld surfaces mapped with two-dimensional (2D) fingerprint plots could reflect the intermolecular interactions in the crystal.[44] By applying one TIBS anion as the center unit, the generated Hirshfeld surfaces showed large red spots in map, indicating its strong intermolecular interactions with the adjacent cations (Figure 3f). Comparatively, by applying one TAPM anion as the center unit in the Hirshfeld surfaces of TPOS-2, there are no red spots, which is a signature of weak interactions with the adjacent cations. The quantitative information on the interactions in the crystal was obtained by plotting 2D fingerprint plots. It's revealed that the intermolecular contact between H and other atoms occupied most of the area in both TPOS-1 and TPOS-2 (Figures S7 and S8). The key difference is that the contribution of H-N interactions in TPOS-1 (33.5%) is significantly higher than in TPOS-2 (24.5%). This indicates that the TPOS-1 scaffold is primarily stabilized by ionic interactions between positively charged protons in the imidazolium cation and negatively charged nitrogen sites in the tetrazolate anion. In contrast, TPOS-2 exhibits a lower contribution of ionic interactions between ammonium cation and tetrazolate anion to stabilization, suggesting the involvement of alternative bonding types, such as a hydrogen-bonding network.

The structural evolution upon POS formation was further probed via nuclear magnetic resonance (NMR) and Fourier transform infrared (FTIR) spectroscopy. Compared to TIBS, all the protons of TPOS-1 showed down-field shift in ^{1}H NMR spectrum (Figure S9). This is due to a decrease in electron density after the protonation of the imidazole group resulting in a deshielded of the ^{1}H nuclei.[45] The ^{19}F NMR spectra (Figure S10) of TPOS-1 exhibited an up-field shift of the fluorine signal from -137.8 and -139.7 ppm after the deprotonation of H_2FBTB fragment. Solid-state NMR (SSNMR) spectra of ^{13}C and ^{11}B cross-polarization magic-angle spinning (CP/MAS) NMR analysis were also acquired and analyzed. The ^{11}B magic angle spinning (MAS) SSNMR spectrum of TIBS exhibited a triplet peak (a sharp center peak with two broad shoulders) centered around 9.7 ppm (Figure S11), indicating the presence of three chemically non-equivalent boron sites. The observed broadening and peak pattern indicate large quadrupolar interactions, along with distinct quadrupolar parameters and isotropic chemical shifts characteristic of the TIBS structure.[46] After forming TPOS-1, one broad peak at 8.8 ppm was observed, indicating that there was only one B environment in TPOS-1. The ^{13}C cross polarization (CP/MAS) SSNMR spectra (Figure S12) showed two carbon signals of TIBS (carbon 2 and 3) that merged into one peak after forming TPOS-1, indicating a more uniform chemical structure in TPOS-1. Similar structural changes and analysis reflected by NMR spectra were observed upon the generation of TPOS-2 (Figures S14-S16). FTIR spectroscopy provided further information on structural changes (Figure S13). The appearance of a peak at 3366 cm^{-1} corresponding to N-H stretching vibration in TPOS-1 was strong evidence that TIBS was protonated, which was not shown in TIBS and H_2FBTB. The N=N (1595 cm^{-1} in H_2FBTB) and C=N (1699, 1616 cm^{-1} in TIBS) stretching exhibited different shift extents after forming TPOS-1 (1637, 1567 cm^{-1}). Besides, the bending of imidazole rings in TIBS also underwent shifts from 1206, 1079 and 922 cm^{-1} to 1169, 1102 and 982 cm^{-1}, respectively. These featured the protonation of the imidazole rings, leading to imidazolium cations formation.[47-48] Similar trend upon the generation of TPOS-2 was also observed and analyzed in Figure S17.

The stability of POSs towards humidity and aqueous environment was then evaluated. To determine and compare the hydrophobicity of the prepared POSs, water vapor adsorption measurements were performed, and both POSs showed an S-type adsorption isotherm (Figure 4a). It has been reported that the hydrophobicity of the framework surface and void can significantly affect the trigging pressure of water vapor adsorption.[35] Under low relative humidity (RH) conditions, the more decisive factor is the interaction between the polar groups distributed in the void channel and water molecules.[49] TPOS-1 exhibited a water adsorption capacity of 92.9 cm^3/g at 298K and 95% RH, with an inflection point at 50% RH. For TPOS-2, the water adsorption capacity was 137.1 cm^3/g at 298 K and 95% RH, with a lower inflection point at 25% RH. Notably, the water uptake capacities of both POSs are significantly lower than those of POSs derived from -SO_3H- and -NH_2-containing monomers, particularly at low RH levels. For instance, at 10% RH, the water adsorption capacities of TPOS-1 and TPOS-2 are 3.6 and 7.8 cm³/g, respectively, which are much lower than the adsorption capacity of POS derived from -SO_3H- and -NH_2-containing monomers, which exceeds 50 cm³/g.[49] At the higher temperature of 313 K, both POSs showed higher inflection points above 60% RH and lower water adsorption capacities (Figure 4b and S18). To gain deeper insight into the water uptake process, isosteric heat of adsorption (ΔH_{ads}) was calculated based on the water vapor adsorption isotherms collected at different temperatures. Under low RH conditions, the average isosteric heat of adsorption (ΔH_1) for TPOS-1 was determined to be 83.66 kJ mol^{-1}. At higher RH, a lower energy requirement (ΔH_2) of 55.08 kJ mol^{-1} was observed for TPOS-1. In contrast, TPOS-2 exhibited more negative isosteric heats of adsorption and stronger interaction strength with H_2O than TPOS-1 in both low- and high-RH regions, with values of 90.39 and 94.64 kJ mol^{-1}, respectively. The structure evolution was elucidated by comparing the PXRD patterns of POSs before and after water vapor adsorption (Figure 4c and 4d). For TPOS-1, no significant changes were observed after water adsorption, with the peaks corresponding to (1,0,-1) crystal planes remaining well preserved. In contrast, the water vapor-saturated TPOS-2 scaffold exhibited significant variations in peak intensity within the 15–25° range, indicating severe phase transition and structural changes. This suggests that although both TPOS-1 and TPOS-2 contain hydrophobic fluorinated tetrazolate units, using imidazolium cations in TPOS-1 provided greater stability compared to TPOS-2, which contains ammonium cations with more active protons for hydrogen bonding network formation.

Small angle neutron scattering (SANS) is powerful for monitoring structural evolution of materials that contain light elements (e.g., C, H, and O).[50] The scattering data of the tectons, TPOSs and deuterium oxide (D_2O)-treated TPOSs were collected using the general-purpose SANS (GP-SANS) diffractometer over a q range of 0.004-0.5 Å^{-1}.[51] The 1D data was obtained after correcting for empty cell scattering, instrument noise,

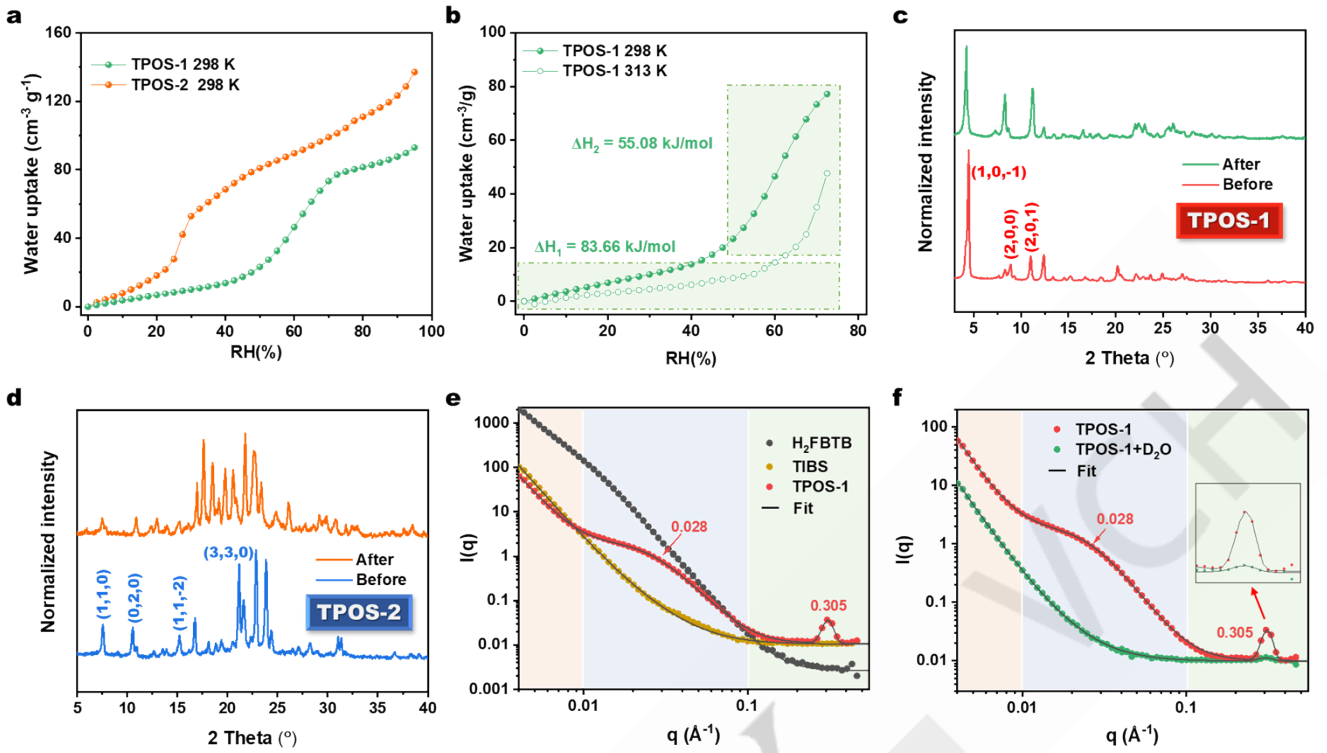

Figure 4. (a) Water vapor adsorption isotherms of TPOS-1 and TPOS-2 at 298 K. (b) Water vapor adsorption isotherms of TPOS-1 at different temperatures and the corresponding isosteric heats of adsorption calculated for two distinct regions. PXRD patterns of TPOS-1 (c) and TPOS-2 (d) before and after water vapor adsorption measurement. (e) Double logarithmic representation of the scattering intensity I(q) of H_2FBTB, TIBS and TPOS-1 obtained by SANS. (f) Double logarithmic representation of the scattering intensity I(q) of dry and D_2O-saturated TPOS-1 obtained by SANS.

transmission and sample thickness by using the drt-SANS. The SANS data of individual tectons, either H_2FBTB or TIBS, fitting can be fitted using a correlation length model with a power law decay (Figure 4e and Table S2). Upon forming TPOS-1, a sharp peak at 0.305 Å^{-1} and a strong shoulder near 0.028 Å^{-1} emerged. The peak at 0.305 Å^{-1} ($2\pi/q$ = 20.6 Å), locating in the high q range (>0.1 Å^{-1}), corresponded to the center-to-center distance of neighboring pores, clearly confirming the presence of uniform microporous channels in TPOS-1. Upon hydration with D_2O, the intensity of the 0.305 Å^{-1} peak significantly decreased but remained detectable (Figure 4f), indicating that the porous channels in TPOS-1 are accessible to D_2O. This property makes it a promising candidate for applications in aqueous media, as it can fully expose the active sites, provided the scaffold remains stable in water. The dry TPOS-1 sample displays a Porod exponent of −4.25, slightly steeper than the ideal −4 expected for a perfectly sharp, smooth interface, implying a gradual scattering-length-density (SLD) transition across the pore–wall boundary (Table S3). After D_2O hydration the exponent moves closer to −4, indicating that water ingress reduces the interfacial gradient and yields a sharper effective interface. In the middle q range (0.001-0.1 Å^{-1}), the shoulder peak seen for the dry TPOS-1 disappeared while the correlation length increased from 100.67 to 178.61 Å after D_2O treatment, implying that D_2O may influence electrostatic interactions with the channel components, thereby altering channel–channel correlations. However, an equally plausible explanation might be simple contrast matching: water uptake smooths out the density inhomogeneity at this length scale in the low q range (<0.001 Å^{-1}), the scattering intensity of TPOS-1 decreased, upon saturation with D_2O, further indicating that the micropores are accessible by D_2O. For TPOS-2, the scatting intensity at low q range also decreased after D_2O treatment, due to reduced contrast between the pores and solid matrix (Figure S19 and Table S4). The Porod exponent changed slightly from 4.02 to 4.11, potentially suggesting the formation of a gradient layer of D_2O. However, no correlation peak corresponding to the center-center distance was observed, as contrast between the two phases drops. These SANS results collectively confirmed that both the external surfaces and internal porous channels of the POSs are accessible to water, while maintaining structural integrity.

The stability of the as-developed POS scaffolds at elevated temperatures and the function of integrated water molecules during crystallization were then studied via variable-temperature (VT) PXRD and theoretical simulations. In the VT-PXRD investigation under N_2 atmosphere, TPOS-1 exhibited very good structural stability in the temperature range of 25-150 °C, with the peak at 2θ = 4.4° corresponding to (1,0,-1) crystal plan well maintained (Figure 5a). In contrast, TPOS-2 underwent obvious structural changes after 75 °C and the peak at 2θ = 7.5° ((1,1,0) crystal plan) became broad and less intense (Figure 5b). It's demonstrated that TPOS-1 possesses better robustness than TPOS-2, and less affected by removing integrated solvent molecules at elevated temperatures. Theoretical simulation was

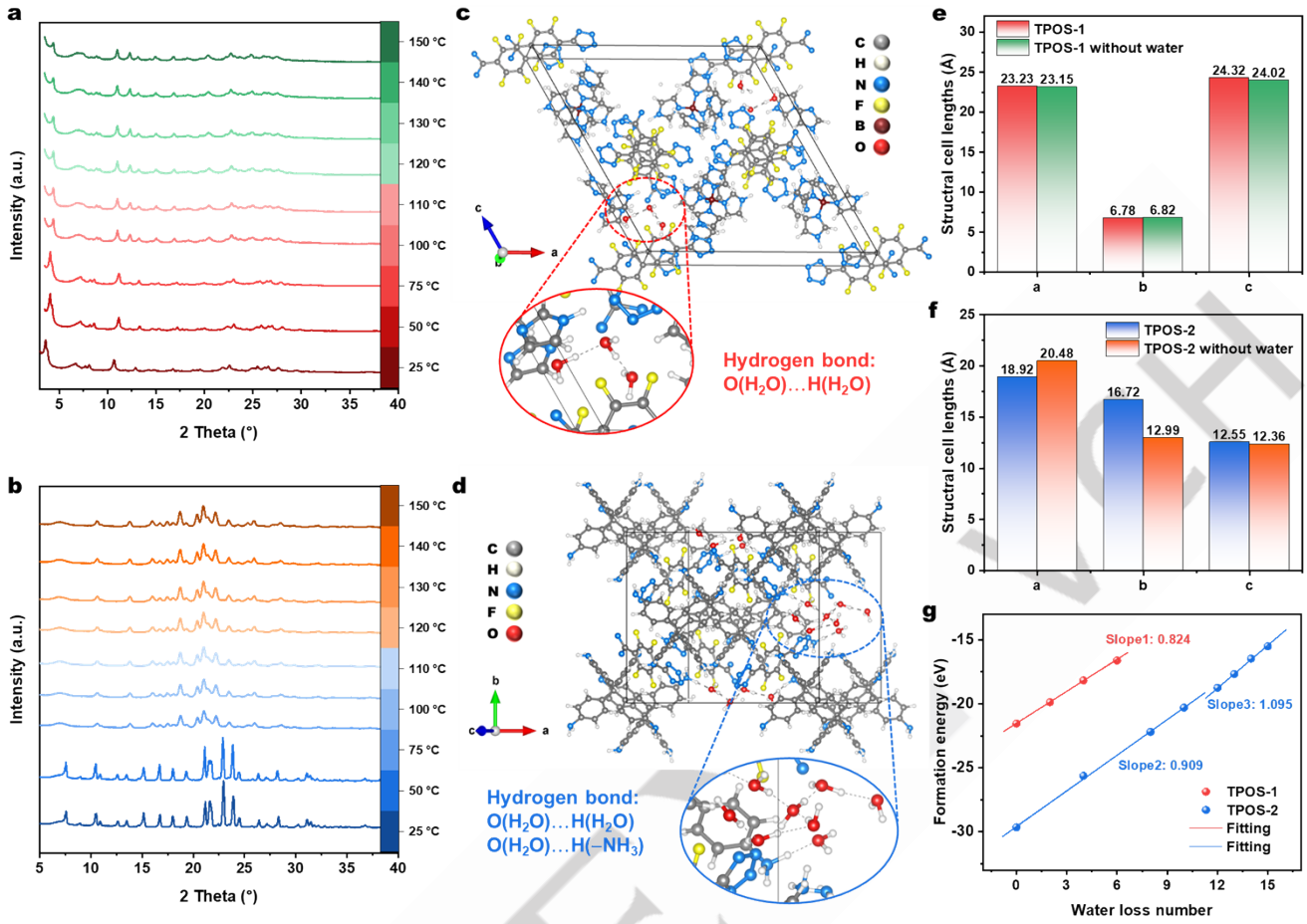

Figure 5. (a) Variable-temperature PXRD patterns of TPOS-1 and (b) TPOS-2 under N_2 atmosphere. (c) DFT-optimized structure of TPOS-1 and (d) TPOS-2, enlarged image highlighting the water molecules-involved hydrogen bonds. (e) Comparison of cell parameters between single crystal of TPOS-1 and DFT-optimized TPOS-1 without water. (f) Comparison of cell parameters between single crystal of TPOS-1 and DFT-optimized TPOS-1 without water. (g) Comparison of formation energies for TPOS-1 and TPOS-2 crystals with different water contents.

then performed to provide fundamental insights into the structure evolution of TPOS-1 and TPOS-2 under water-lean environment. The initial models of POSs with integrated H_2O molecules within the scaffolds are built based on single-crystal structures and the amount of water molecules was determined by thermal gravimetric analysis (TGA) (Figures S20-S22). The XRD patterns of the simulated models are consistent with the experimental results (Figures S23 and S24). Notably, in the optimized structures, the existing form of water molecules and hydrogen bonding differ significantly between TPOS-1 and TPOS-2. In TPOS-1, hydrogen bonding occurs exclusively between water molecules (as water clusters), with no apparent interaction between water and the scaffold (Figure 5c). In contrast, TPOS-2 exhibits extensive hydrogen bonding between water molecules and ammonium cations within the scaffolds (Figure 5d). Subsequently, water molecules are removed from the model scaffolds and then structure optimization is performed to obtain water-lean structures. For TPOS-1 (Figures S23 and S25), no significant structural differences were observed, as reflected in the nearly unchanged PXRD patterns and unit cell lengths compared to the original single-crystal structure (Figure 5e). In contrast, the PXRD pattern of TPOS-2 became entirely different (Figure S24), even though the stacking of the tectons remained unchanged (Figure S26). Before and after the removal of water molecules, the unit cell lengths of TPOS-2 also underwent noticeable changes, with *a* axis scale length increasing from 18.92 to 20.48 Å and the *b* axis decreasing from 16.72 to 12.99 Å (Figure 5f). This indicates that water molecules play an indispensable role in the framework construction of TPOS-2, while their influence on TPOS-1 is minimal. The significantly reduced dependence on water for maintaining the intact structure of the TPOS-1 scaffold, compared to its critical role in TPOS-2, is further elucidated by the relationship between formation energy changes and the integrated amount of water molecules (Figure 5g). For TPOS-1 crystals with different water contents, the formation energies follow a linear trend with a slope of 0.824, indicating minimal structural changes upon dehydration. This suggests a weak response to water, consistent with its hydrophobic nature. In contrast, TPOS-2 crystals exhibit two distinct linear segments in formation energy, indicating structural

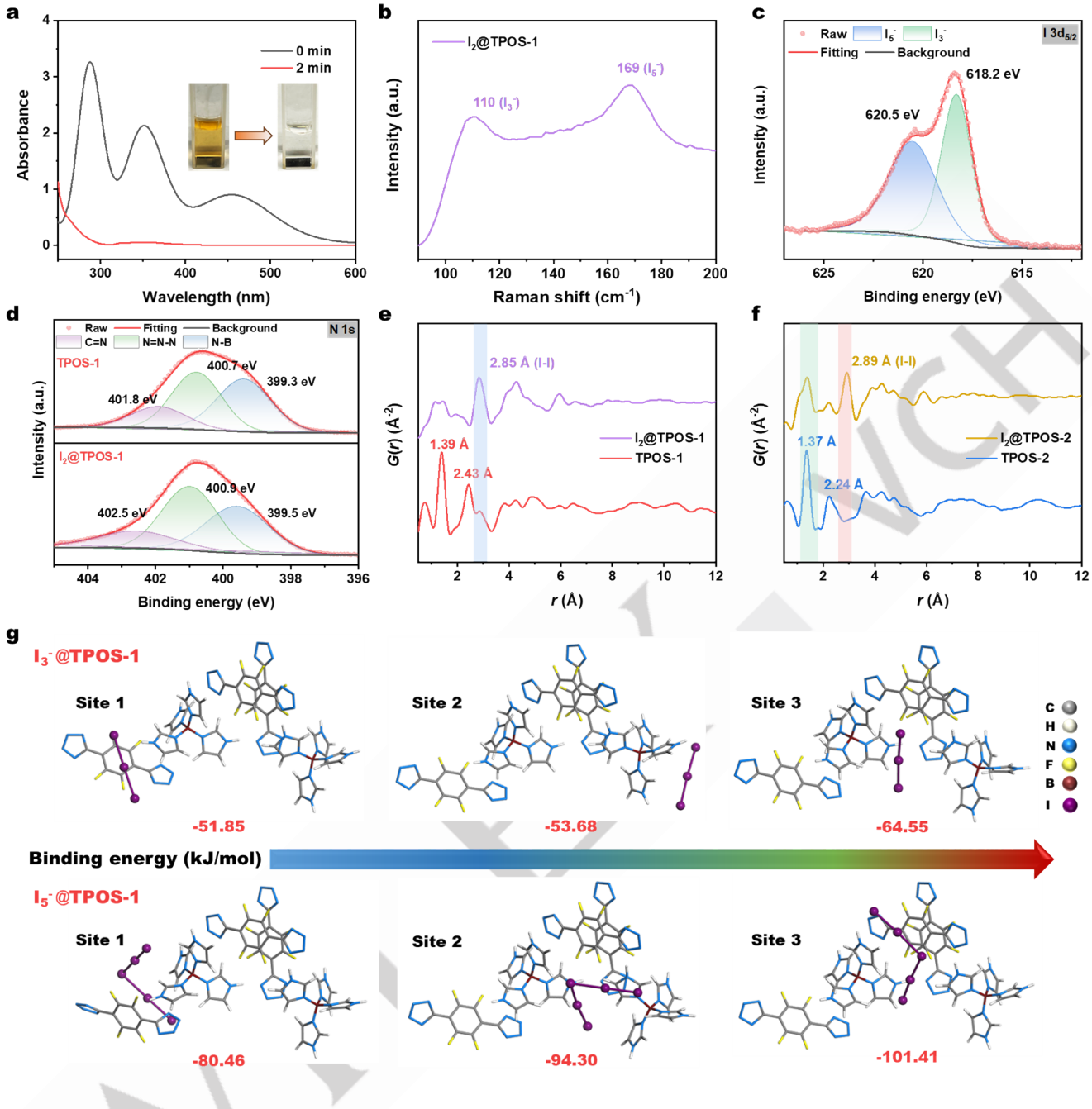

Figure 6. (a) UV/vis spectra and insert optical images of saturated iodine aqueous solution (1.2 mM) before and after adding TPOS-1 adsorbent (3.0 mg). (b) Raman spectra of TPOS-1 before and after iodine adsorption. (c) I 3d XPS spectrum of TPOS-1 after iodine adsorption. (d) N 1s XPS spectra of TPOS-1 before and after iodine adsorption. Atomic pair distribution functions (PDF) of TPOS-1(e) and TPOS-2(f) before and after iodine adsorption. (g) Computed binding energies of iodine species with TPOS-1 in different sites.

changes upon dehydration. The steeper slope (slope3: 1.095) reflects strong water–structure interactions, making TPOS-2 more sensitive to water.

The highly polar pore channels, abundant electron-rich moieties such as heteroatoms and π-systems (aromatic and tetrazole rings), along with the excellent water and thermal stability of TPOS, promoted us to investigate its potential for iodine capture in aqueous solutions.[52]] To assess this capability, TPOSs were employed as adsorbents in a saturated iodine aqueous solution (1.2 mM). Optical images revealed a significant reduction of iodine concentration within just 2 min of adding TPOS-1, a result further confirmed by UV-vis spectra, which indicated a removal efficiency exceeding 95% (Figure 6a). Similarly, TPOS-2 exhibited good iodine removal efficiency in aqueous solutions (Figure S27). The maximum iodine adsorption capacities in aqueous solutions for TPOS-1 and TPOS-2 were determined to be 0.33 g/g and 0.12 g/g, respectively, based on elemental analysis of iodine-saturated samples. To gain deep

insight into the adsorption process and identify the adsorbed iodine species, Raman spectroscopy, X-ray photoelectron spectroscopy (XPS) and solid-state ^{13}C CPMAS NMR were utilized to characterize the I_2-loaded samples. As shown in Figure 6b, two characteristic peaks at 169 cm^{-1} and 110 cm^{-1} appeared for I_2-loaded TPOS-1 (I_2@TPOS-1) compared to pure TPOS-1. Specifically, the characteristic peak at 169 cm^{-1} corresponded to the stretching vibration of polyiodide species I_5^-, while the peak at 110 cm^{-1} could be assigned to the symmetric stretching of I_3^-. The peaks at 618.2 eV and 620.5 eV in the I3d XPS spectrum further confirmed that iodine is adsorbed by TPOS-1 in the forms of I_3^- and I_5^- (Figure 6c). In the N 1s XPS spectra (Figure 6d), it's observed that the peak attributed to the C=N bond shifted from 402.5 eV to 401.8 eV after iodine adsorption. This indicates a strong interaction between the positively charged imidazole groups in TPOS-1 and iodine. This conclusion is also reflected in the solid-state ^{13}C CPMAS NMR and FTIR results: the carbon peak at 121.0 ppm corresponding to the imidazole group exhibited down-field shift to 123.5 ppm after loading iodine (Figure S28); the characteristic peak of C=N stretching red-shifted from 1637 cm^{-1} to 1650 cm^{-1} (Figure S29). Similar observations and analyses for TPOS-2 are provided in the supporting information (Figures S30–S34). The results indicate that the iodine captured by TPOS-2 also consists of I_3^- and I_5^- species, with the primary adsorption sites being the charged amine groups, driven by hydrogen bonding.

The excellent recyclability of TPOS-1 is evidenced by its retention of 93% iodine removal efficiency after five consecutive regeneration cycles in methanol (Figure S35). Furthermore, the recycled TPOS-1 preserved its structural integrity, as evidenced by its consistent PXRD patterns compared to pristine TPOS-1 (Figure S36). In comparison with the original PDF of TPOS-1, the post-adsorption PDF exhibited a pronounced new peak at 2.85 Å (Figures 6e and S37), while retaining the positions of the original peaks. This additional peak is attributed to the I–I bond length of the adsorbed iodine species.[53] However, for the iodine-loaded TPOS-2 (I_2@TPOS-2), its structural instability was reflected in altered PXRD patterns and reduced intensity following iodine capture and release (Figure S38),along with the appearance of a distinct I–I bond peak at 2.89 Å in the PDF (Figure 6f and S39).

DFT calculations were further conducted to investigate the mechanism of iodine capture. Independent models were employed to illustrate non-covalent interactions, including different adsorption sites and binding energies. For TPOS-1 model consisting of three H_2FBTB and two TIBS units without sodium moieties (Figure 6g), the binding energy of the I_3^- species ranged from -51.85 to -64.55 kJ mol^{-1}, with adsorption sites primarily located at the N-H groups on the imidazole groups and the C–F functionalizations on the anions. These interactions were predominantly driven by charge transfer and Coulomb interactions with the electron-deficient I_3^- species. In contrast, the I_5^- species exhibited a higher binding energy, ranging from -80.46 to -101.41 kJ/mol, with the dominant adsorption sites similarly being the N-H groups and aromatic rings. Compared to TPOS-1, both I_3^- and I_5^- exhibited relatively lower binding energies with TPOS-2, ranging from -36.11 to -44.77 kJ/mol and -53.60 to -69.36 kJ/mol, respectively (Figure S40). The primary adsorption sites in TPOS-2 were the protonated amine groups on the cations and the C–F functionalizations on the anions, with the driving forces involving hydrogen bonding between the iodine species and amine groups, as well as charge transfer interactions with the π-systems. These findings indicate that the higher iodine adsorption capacity of TPOS-1 can be attributed to its stronger affinity for the charged iodine species.

Conclusion

In summary, we developed a facile and efficient approach to construct POS scaffolds with exceptional robustness and structural integrity independent of water molecules. The key innovation lies in using fluorinated tetrazole as a weak acid tecton and a tetra-substituted imidazole monomer as the base counterpart. The resulting POS material, synthesized via neutralization, features hydrophobic channels and minimal hydrogen bonding within the scaffold. Single-crystal analysis and computational modeling confirmed that trapped water molecules exist as clusters, with hydrogen bonding occurring only between water molecules, not with the POS scaffold. The stability of POS material was demonstrated under both aqueous and water-lean conditions, withstanding high temperatures without changes in stacking mode or crystal structure. This superior stability of POS material enables its high-capacity and recyclable iodine capture in aqueous media. The design and synthesis strategy presented here represents a significant advancement in extending the applicability of POS materials under both humid and dry conditions.

Supporting Information

Supporting Information is available from the Wiley Online Library or from the author.

Acknowledgements

The research was supported financially by the Division of Chemical Sciences, Geosciences, and Biosciences, Office of Basic Energy Sciences, US Department of Energy. This research used resources at the High Flux Isotope Reactor, a DOE Office of Science User Facility operated by the Oak Ridge National Laboratory (IPTS-33565 and 32388). This research was performed on APS beam time award: https://doi.org/10.46936/APS-188511/60013158, from the Advanced Photon Source, a U.S. Department of Energy (DOE) Office of Science user facility operated for the DOE Office of Science by Argonne National Laboratory under Contract No. DE-AC02-06CH11357.

Conflict of Interest

The authors declare no conflict of interest.

Data Availability Statement

The data that support the findings of this study are available in the supplementary material of this article.

Keywords: Porous organic salts • Fluorinated tecton • Hydrogen bonding • Water stability • Thermal stability

References

[1] J. Jiao, W. Gong, X. Wu, S. Yang, Y. Cui, *Coord. Chem. Rev.* **2019**, *385*, 174-190.
[2] L. Kong, M. Zhong, W. Shuang, Y. Xu, X.-H. Bu, *Chem. Soc. Rev.* **2020**, *49*, 2378-2407.
[3] L. Liu, A. Corma, *Nat. Rev. Mater.* **2021**, *6*, 244-263.
[4] G. Ding, J. Zhao, K. Zhou, Q. Zheng, S.-T. Han, X. Peng, Y. Zhou, *Chem. Soc. Rev.* **2023**.
[5] Y. Tian, G. Zhu, *Chem. Rev.* **2020**, *120*, 8934-8986.
[6] O. M. Yaghi, M. O'Keeffe, N. W. Ockwig, H. K. Chae, M. Eddaoudi, J. Kim, *Nature* **2003**, *423*, 705-714.
[7] H. Furukawa, K. E. Cordova, M. O'Keeffe, O. M. Yaghi, *Science* **2013**, *341*, 1230444.
[8] *Chem. Rev.* **2012**, *112*, 673-674.
[9] E. G. Percástegui, T. K. Ronson, J. R. Nitschke, *Chem. Rev.* **2020**, *120*, 13480-13544.
[10] F. J. Rizzuto, L. K. von Krbek, J. R. Nitschke, *Nat. Rev. Chem.* **2019**, *3*, 204-222.
[11] S.-Y. Ding, W. Wang, *Chem. So. Rev.* **2013**, *42*, 548-568.
[12] C. S. Diercks, O. M. Yaghi, *Science* **2017**, *355*, eaal1585.
[13] K. T. Tan, S. Ghosh, Z. Wang, F. Wen, D. Rodríguez-San-Miguel, J. Feng, N. Huang, W. Wang, F. Zamora, X. Feng, A. Thomas, D. Jiang, *Nat. Rev. Methods Primers* **2023**, *3*, 1.
[14] Z. Wang, S. Zhang, Y. Chen, Z. Zhang, S. Ma, *Chem. Soc. Rev.* **2020**, *49*, 708-735.
[15] L. Chen, B. Zhang, L. Chen, H. Liu, Y. Hu, S. Qiao, *Mater. Adv.* **2022**, *3*, 3680-3708.
[16] R.-B. Lin, B. Chen, *Chem* **2022**, *8*, 2114-2135.
[17] Y. Yang, L. Li, R.-B. Lin, Y. Ye, Z. Yao, L. Yang, F. Xiang, S. Chen, Z. Zhang, S. Xiang, *Nat. Chem.* **2021**, *13*, 933-939.
[18] T. Tozawa, J. T. Jones, S. I. Swamy, S. Jiang, D. J. Adams, S. Shakespeare, R. Clowes, D. Bradshaw, T. Hasell, S. Y. Chong, C. Tang, S. Thompson, J. Parker, A. Trewin, J. Bacsa, A. M. Z. Slawin, A. Steiner, A. I. Cooper, *Nat. Mater.* **2009**, *8*, 973-978.
[19] X. Yang, Z. Ullah, J. F. Stoddart, C. T. Yavuz, *Chem. Rev.* **2023**, *123*, 4602-4634.
[20] M. Liu, L. Zhang, M. A. Little, V. Kapil, M. Ceriotti, S. Yang, L. Ding, D. L. Holden, R. Balderas-Xicohténcatl, D. He, R. Clowes, S. Y. Chong, G. Schütz, L. Chen, M. Hirscher, A. I. Cooper, *Science* **2019**, *366*, 613-620.
[21] S.-Y. Zhang, Z. Kochovski, H.-C. Lee, Y. Lu, H. Zhang, J. Zhang, J.-K. Sun, J. Yuan, *Chem. Sci.* **2019**, *10*, 1450-1456.
[22] T. Tozawa, J. T. Jones, S. I. Swamy, S. Jiang, D. J. Adams, S. Shakespeare, R. Clowes, D. Bradshaw, T. Hasell, S. Y. Chong, C. Tang, S. Thompson, J. Parker, A. Trewin, J. Bacsa, A. M. Slawin, A. Steiner, A. I. Cooper, *Nat. Mater.* **2009**, *8*, 973-978.
[23] S. Yu, G. L. Xing, L. H. Chen, T. Ben, B. L. Su, *Adv. Mater.* **2020**, *32*, e2003270.
[24] G. Xing, D. Peng, T. Ben, *Chem. Soc. Rev.* **2024**, *53*, 1495-1513.
[25] H. Sei, K. Oka, Y. Hori, Y. Shigeta, N. Tohnai, *Chem. Sci.* **2024**, *15*, 8008-8018.
[26] A. Karmakar, R. Illathvalappil, B. Anothumakkool, A. Sen, P. Samanta, A. V. Desai, S. Kurungot, S. K. Ghosh, *Angew. Chem. Int. Ed.* **2016**, *55*, 10667-10671; *Angew. Chem.* **2016**, *128*, 10825-10829.
[27] I. Brekalo, D. E. Deliz, L. J. Barbour, M. D. Ward, T. Friščić, K. T. Holman, *Angew. Chem. Int. Ed.* **2020**, *59*, 1997-2002; *Angew. Chem.* **2020**, *132*, 2013-2018.
[28] M. Morshedi, M. Thomas, A. Tarzia, C. J. Doonan, N. G. White, *Chem. Sci.* **2017**, *8*, 3019-3025.
[29] G. Xing, T. Yan, S. Das, T. Ben, S. Qiu, *Angew. Chem. Int. Ed.* **2018**, *57*, 5345-5349; *Angew. Chem.* **2018**, *130*, 5443-5447.
[30] M. O'Shaughnessy, J. Glover, R. Hafizi, M. Barhi, R. Clowes, S. Y. Chong, S. P. Argent, G. M. Day, A. I. Cooper, *Nature* **2024**, *630*, 102-108.
[31] Q. Mao, S. Yang, J. Zhang, Y. Liu, M. Liu, *Adv. Sci.* **2024**, e2408494.
[32] M. Liu, L. Chen, S. Lewis, S. Y. Chong, M. A. Little, T. Hasell, I. M. Aldous, C. M. Brown, M. W. Smith, C. A. Morrison, L. J. Hardwick, A. I. Cooper, *Nat. Commun.* **2016**, *7*, 12750.
[33] Y. Sheng, Q. Chen, J. Yao, Y. Lu, H. Liu, S. Dai, *Angew. Chem. Int. Ed.* **2016**, *55*, 3378-3381; *Angew. Chem.* **2016**, *128*, 3439-3442.
[34] M. O'Shaughnessy, A. C. Padgham, R. Clowes, M. A. Little, M. C. Brand, H. Qu, A. G. Slater, A. I. Cooper, *Chem. Eur. J.* **2023**, *29*, e202302420.
[35] T. Ami, K. Oka, S. Kitajima, N. Tohnai, *Angew. Chem. Int. Ed.* **2024**, *63*, e202407484; *Angew. Chem.* **2024**, *136*, e202407484.
[36] Z. Zhang, O. Š. Miljanić, *Org. Mater.* **2019**, *01*, 019-029.
[37] T. Ami, K. Oka, K. Tsuchiya, N. Tohnai, *Angew. Chem. Int. Ed.* **2022**, *61*, e202202597; *Angew. Chem.* **2022**, *134*, e202202597.
[38] W. Xin, J. Fu, Y. Qian, L. Fu, X.-Y. Kong, T. Ben, L. Jiang, L. Wen, *Nat. Commun.* **2022**, *13*, 1701.
[39] M. Busch, E. Ahlberg, E. Ahlberg, K. Laasonen, *ACS Omega* **2022**, *7*, 17369-17383.
[40] D. T. Manallack, *Perspect. Med. Chem.* **2007**, *1*, 25-38.
[41] H. Zhu, Y. Huang, J. Ren, B. Zhang, Y. Ke, A. K. Y. Jen, Q. Zhang, X. L. Wang, Q. Liu, *Adv. Sci.* **2021**, *8*, 2003534.
[42] S. D. Jacques, M. Di Michiel, S. A. Kimber, X. Yang, R. J. Cernik, A. M. Beale, S. J. Billinge, *Nat. Commun.* **2013**, *4*, 2536.
[43] M. W. Terban, S. J. Billinge, *Chem. Rev.* **2021**, *122*, 1208-1272.
[44] P. R. Spackman, M. J. Turner, J. J. McKinnon, S. K. Wolff, D. J. Grimwood, D. Jayatilaka, M. A. Spackman, *J. Appl. Cryst.* **2021**, *54*, 1006-1011.
[45] C. Kasireddy, J. G. Bann, K. R. Mitchell-Koch, *Phys. Chem. Chem. Phys.* **2015**, *17*, 30606-30612.
[46] J. Dosso, H. Oubaha, F. Fasano, S. Melinte, J.-F. Gohy, C. E. Hughes, K. D. Harris, N. Demitri, M. Abrami, M. Grassi, *Chem. Mater.* **2022**, *34*, 10670-10680.
[47] A. R. Lara-Hernández, N. V. Gallardo-Rivas, U. Páramo-García, R. Mayen-Mondragon, S. B. Brachetti-Sibaja, *Int. J. Electrochem. Sci.* **2021**, *16*.
[48] C. Zhao, X. Qiao, Z. Yi, Q. Guan, W. Li, *Phys. Chem. Chem. Phys.* **2020**, *22*, 2849-2857.
[49] S. Zhang, J. Fu, S. Das, K. Ye, W. Zhu, T. Ben, *Angew. Chem. Int. Ed.* **2022**, *61*, e202208660; *Angew. Chem.* **2022**, *134*, e202208660.
[50] X. Wang, L. He, J. Sumner, S. Qian, Q. Zhang, H. O'Neill, Y. Mao, C. Chen, A. M. Al-Enizi, A. Nafady, S. Ma, *Nat. Commun.* **2023**, *14*, 973.
[51] W. T. Heller, M. Cuneo, L. Debeer-Schmitt, C. Do, L. He, L. Heroux, K. Littrell, S. V. Pingali, S. Qian, C. Stanley, V. S. Urban, B. Wu, W. Bras, *J. Appl. Cryst.* **2018**, *51*, 242-248.
[52] K. Jie, Y. Zhou, Q. Sun, B. Li, R. Zhao, D.-e. Jiang, W. Guo, H. Chen, Z. Yang, F. Huang, *Nat. Commun.* **2020**, *11*, 1086.
[53] D. F. Sava, M. A. Rodriguez, K. W. Chapman, P. J. Chupas, J. A. Greathouse, P. S. Crozier, T. M. Nenoff, *J. Am. Chem. Soc.* **2011**, *133*, 12398-12401.
[54] Deposition Number 2414197 for TPOS-1 and 2414198 for TPOS-2 contain the supplementary crystallographic data

for this paper. These data are provided free of charge by the joint Cambridge Crystallographic Data Centre and Fachinformationszentrum Karlsruhe Access Structures service.

Entry for the Table of Contents

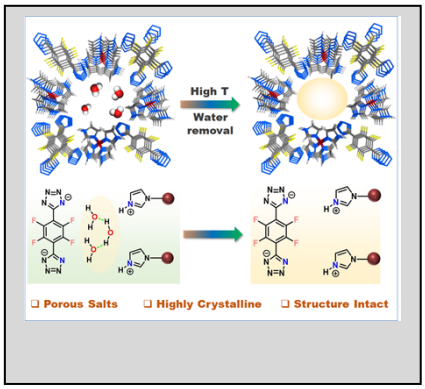

Porous organic salts featuring hydrophobic channels and minimal hydrogen bonding were constructed using a fluorinated tetrazole as a weak acid tecton and a tetra-substituted imidazole precursor lacking active protons as the base. These materials exhibited exceptional robustness and structural integrity under both aqueous and water-lean conditions, maintaining their stacking mode and crystal structure even at elevated temperatures.